

RESEARCH ARTICLE

2D MATERIALS

Perfect Coulomb drag in a dipolar excitonic insulator

Phuong X. Nguyen^{1,2†}, Ligu Ma^{1†‡}, Raghav Chaturvedi^{1†}, Kenji Watanabe³, Takashi Taniguchi³, Jie Shan^{1,2,4*}, Kin Fai Mak^{1,2,4*}

Excitonic insulators (EIs) are a solid-state prototype for bosonic phases of matter that can support charge-neutral exciton currents. However, demonstration of exciton transport in EIs is difficult. In this work, we show that the strong interlayer excitonic correlation at equal electron and hole densities in MoSe₂/WSe₂ double layers separated by a 2-nanometer barrier yields perfect Coulomb drag under zero magnetic field: A charge current in one layer induces an equal but opposite drag current in the other layer at low temperatures. The drag current ratio remains above 0.9 up to about 20 kelvin. As exciton density increases above the Mott density, the excitons dissociate into an electron-hole plasma abruptly, and only frictional drag is observed. Our experiment may lead to the realization of exciton circuitry and superfluidity.

Excitonic insulators (EIs) arise in semiconductors when the electron-hole binding energy exceeds the bandgap (1, 2). Unlike the charged excitations that are frozen and unable to transport current, the neutral electron-hole pairs (excitons) are free to move in EIs. However, it is intrinsically difficult to demonstrate exciton transport in bulk EI candidates because separate electrical contacts cannot be made to the electrons and holes. This difficulty is overcome in Coulomb-coupled electron-hole double layers. Perfect Coulomb drag—a manifestation of pure exciton transport—has been demonstrated in Coulomb-coupled quantum wells (3–5) and graphene double layers (6–9) but only in the quantum Hall regime. The electron-hole binding becomes negligible in the absence of a magnetic field in these systems; only a frictional and/or energy drag has been reported (10–14). The recently discovered dipolar EIs based on Coulomb-coupled atomic double layers (15, 16) open the possibility to realize perfect Coulomb drag under zero magnetic field. The strong exciton binding and the dispersive excitonic band in this system also present an unexplored regime for the studies of exciton transport (17–20).

The dipolar EI of interest is realized in double-layer structures made of two semiconducting transition metal dichalcogenide (TMD) monolayers that support a type-II band alignment (15, 16, 21–25) (Fig. 1A). The two TMD mono-

layers, which are separated by a thin dielectric spacer, are separately contacted by metallic electrodes and form the two plates of a parallel-plate capacitor (Fig. 1B). The application of an interlayer bias voltage V_b splits the electron and hole chemical potentials by eV_b and reduces the charge gap to $\varepsilon_G - eV_b$ for quasiparticle excitations from the zero-bias bandgap ε_G of the double layer (Fig. 1A). (Here, e is the elementary charge.) When the charge gap becomes smaller than the exciton binding energy, $\varepsilon_G - eV_b < \varepsilon_b$, spontaneous formation of dipolar (interlayer) excitons is favorable (1, 26, 27). An EI has been demonstrated by recent thermodynamic measurements (15, 16). The platform provides an opportunity to realize strongly correlated bosonic phases of matter (21, 28–35). The separate electron and hole contacts to the EI, which are lacking in bulk EI candidates (36–41), also provide an electrical reservoir for dipolar excitons with continuously tunable density n_x and chemical potential eV_b (22, 23).

The Coulomb drag effect is a sensitive probe of the correlation effect between two spatially separated conductors (42). The Coulomb interactions between the two layers enable an electric current flowing in one layer (I_{drive}) to induce a drag current (I_{drag}) in the other layer if the second layer is part of a closed circuit (Fig. 1C). Similarly, a voltage drop (V_{drag}) is developed if the second layer is an open circuit (Fig. 1D). We show perfect Coulomb drag in the dipolar EI based on TMD electron-hole double layers at low temperatures; a large drag current ratio remains above 0.9 up to about 20 K. We also demonstrate an equilibrium exciton Mott transition, in contrast to earlier studies of the transition under nonequilibrium settings, such as under optical pumping (43, 44).

Device operation and EI

Our sample consists of Coulomb-coupled MoSe₂/WSe₂ double layers with nearly symmetric top

and bottom gates (Fig. 1B). Details of the device design and fabrication are described in the supplementary materials (45). Compared with the earlier compressibility study (15), multiple contacts to each TMD layer with substantially reduced contact resistances have been fabricated. The devices are divided into the channel and contact regions, in which the two TMD monolayers are separated by thin (5 to 6 layers) and thick (10 to 20 nm) hexagonal boron nitride (hBN) spacers, respectively. The TMDs are angle-misaligned to further suppress interlayer tunneling in the channel region. The MoSe₂ (Mo) and WSe₂ (W) layers are contacted by bismuth and platinum electrodes for electron and hole transport, respectively. The interlayer bias voltage V_b is applied to inject electron-hole pairs into the channel and tune the pair density n_p . The top and bottom gate voltages (V_{tg} and V_{bg} , respectively) further allow independent control of the electron-hole density imbalance in the double layer through the symmetric combination, $V_g = (V_{\text{tg}} + V_{\text{bg}})/2$, and the perpendicular electric field through the antisymmetric combination, $\Delta = (V_{\text{bg}} - V_{\text{tg}})/2$. In the channel region, the electric field reduces the bandgap; however, in the contact regions, because of the much thicker hBN spacer, the electric field heavily electron (hole) dopes the Mo (W) layer to substantially reduce the metal-semiconductor junction resistances. Junction resistances on the order of several kilohms at 1.5 K have been achieved. The contact regions are thus charge reservoirs for exciton injection into the channel region (15).

We identify the EI phase of the double layer using the capacitance measurements (fig. S2) as reported in an earlier study (15). Both the penetration capacitance (C_p , capacitance between the two gates) and the interlayer capacitance (C_i , capacitance between the TMD monolayers) are measured as a function of V_g and V_b at $\Delta = 5.5$ V and 1.5 K. They characterize the charge and exciton compressibilities (15), respectively. Figure 2A illustrates C_p normalized by its geometric value (C_{gg}). The large penetration capacitance at small bias voltages marks the *ii* region, with both layers being charge neutral. Its boundary, denoted by two black dashed lines, traces the band edge of the electron and hole layers (the band edge of the hole layer is fixed at $V_g = 0$ because the hole layer is grounded). Varying the gate voltage across each boundary introduces doping in one of the layers (the *pi* and *in* regions). For sufficiently large bias voltages, both layers are doped (the *pn* region). Further, the simultaneous interlayer capacitance measurement (fig. S2B) identifies the dash-dotted line, above which the electron-hole pairs are injected into the channel. The enclosed triangular region is an EI, which is charge insulating at low temperatures but hosts an equilibrium dipolar exciton fluid. The exciton binding energy,

¹School of Applied and Engineering Physics, Cornell University, Ithaca, NY, USA. ²Kavli Institute at Cornell for Nanoscale Science, Ithaca, NY, USA. ³National Institute for Materials Science, Tsukuba, Japan. ⁴Laboratory of Atomic and Solid State Physics, Cornell University, Ithaca, NY, USA.

*Corresponding author. Email: jie.shan@cornell.edu (J.S.); kinfai.mak@cornell.edu (K.F.M.)

†These authors contributed equally to this work.

‡Present address: Zhejiang Key Laboratory of Micro-nano Quantum Chips and Quantum Control, School of Physics, Zhejiang University, Hangzhou, China.

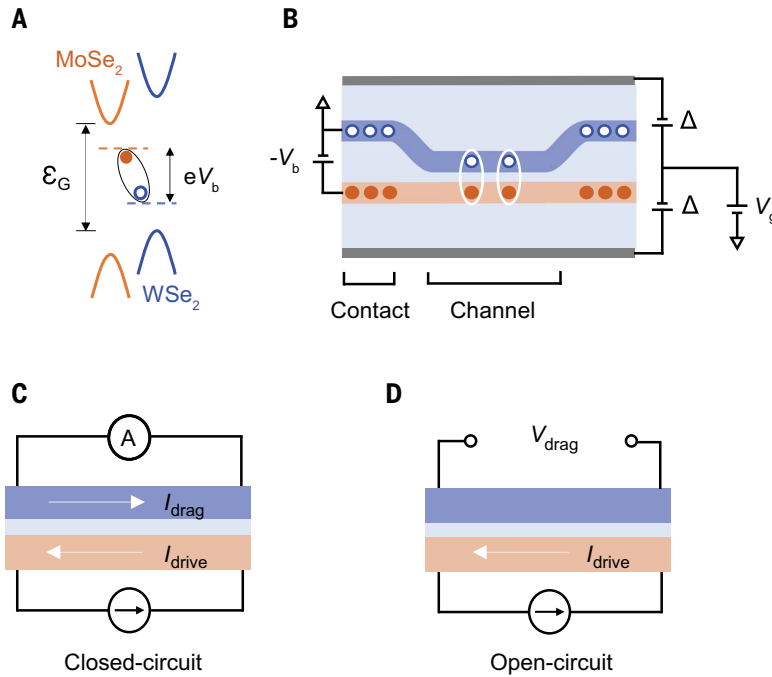


Fig. 1. Coulomb drag measurements in a dipolar EI. (A) Type-II band alignment of MoSe₂/WS₂ heterostructures with an interlayer bandgap ϵ_G . An interlayer bias voltage V_b is applied to separate the electron (filled circle) and hole (empty circle) chemical potentials. An EI spontaneously forms when the charge gap, $\epsilon_G - eV_b$, is smaller than the exciton binding energy ϵ_b . (B) Cross-sectional schematic of dual-gated WS₂/hBN/MoSe₂ transport devices. The W layer, Mo layer, graphite gates, and hBN dielectrics are colored in blue, orange, gray, and light blue, respectively; V_g and Δ are the symmetric and antisymmetric combinations of the top and bottom gate voltages. Under a large perpendicular electric field $\propto \Delta$, the contact regions with a thick hBN spacer (~ 10 to 20 nm) are heavily doped with free electrons and holes, allowing exciton injection into the channel region with a thin BN spacer (~ 2 nm). (C and D) Schematic for the closed-circuit (C) and open-circuit (D) drag measurements. A bias current I_{drive} is applied to the Mo layer. The W contacts are shorted through an ammeter to measure the drag current I_{drag} in (C) and are connected to a voltmeter to measure the open-circuit drag voltage V_{drag} in (D).

$\epsilon_b \approx 30$ meV, is approximately given by the difference between the bias voltage at the tip of the triangle (0.52 V), beyond which the excitons dissociate into free electrons and holes, and the base of the triangle (0.49 V), at which excitons are just injected into the double-layer channel. The channel bandgap ϵ_G is reduced from the intrinsic value of 1.6 eV to 0.52 eV by antisymmetric gating Δ .

Perfect Coulomb drag

We study Coulomb drag in our devices using the drag counterflow geometry (Fig. 1C). We drive an electron current in the Mo layer using a small ac in-plane bias (5 to 10 mV) and measure the drag current in the W layer (45). Figure 2, B and C, shows the V_g and V_b dependences of the drive and drag currents at 1.5 K (see fig. S3 for results from driving the W layer). As expected, a finite I_{drive} is observed whenever the Mo layer is turned on—that is, in the *in*, *pn*, and EI regions. The current increases with increasing electron density. The discrepancy between the transport and capacitance results near the Mo band edge in the *in* region (with small V_b) is likely related to the large contact resistance in the Mo layer (45) (fig. S5). By contrast, a I_{drag} hotspot is observed only near the EI region; it decays rapidly with both increasing V_b and V_g , which increase the exciton density and the electron-hole density imbalance, respectively. In addition, I_{drag} always flows in the opposite direction of I_{drive} (fig. S4).

Below, we focus on the case of equal electron and hole densities in the double layer (along the white dashed line in Fig. 2A). The more general case of a finite electron-hole density

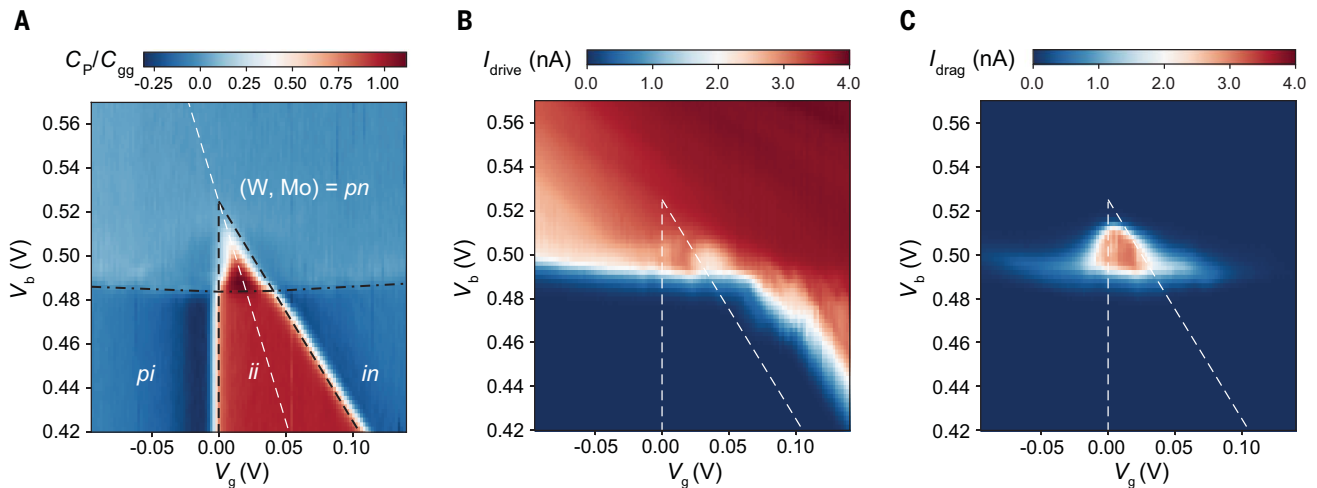


Fig. 2. Exciton transport and electrostatics phase diagram. (A) Normalized penetration capacitance C_P/C_{gg} as a function of V_b and V_g , where C_{gg} is the gate-to-gate geometric capacitance. The five distinct regions are separated by the black dashed and dash-dotted lines; the dashed lines correspond to the TMD band edges [see (15) for details]. Here *i*, *p*, and *n* denote, respectively, an intrinsic, hole-doped, and electron-doped layer. The double layer is incompressible in the *ii* region, where both layers are intrinsic, and in the EI region (the triangular area enclosed by

the black dashed and dash-dotted lines), where an equilibrium exciton fluid emerges. The white dashed line marks equal electron and hole densities. (B and C) Drive current in the Mo layer (B) and drag current in the W layer (C) as a function of V_b and V_g . The white dashed lines are reproduced from the black dashed lines in (A). The Mo layer is turned on in the *in*, *pn*, and EI regions. Large drag current is observed in the EI region. A weaker drag current is also observed in a slightly electron- and hole-doped EI. All measurements were carried out at 1.5 K.

imbalance, involving a Bose-Fermi mixture (46, 47) and screened excitonic interactions, is responsible for the nonzero I_{drag} outside the EI region and will be examined in future studies. Figure 3A shows the current amplitude in two layers at 1.5 K as a function of V_b or n_p . The pair density is obtained from the interlayer capacitance measurement $n_p = \int \frac{C_1}{e} dV_b$ (fig. S2C). The drive current turns on sharply at $V_b \approx (\epsilon_G - \epsilon_b)/e$, when excitons are first injected into the channel, followed by a moderate increase with increasing V_b . The small deviations of the drive current from a smooth monotonic V_b dependence are device specific and are likely related to the junction imperfections. Notably, I_{drag} is nearly identical to I_{drive} (but with opposite direction) until the bias reaches a threshold $V_b \approx \epsilon_G/e$, beyond which I_{drag} vanishes abruptly. The corresponding pair density is the Mott limit, $n_M \approx 4.0 \times 10^{11} \text{ cm}^{-2}$ (see fig. S17 for calibration). Figure 3A also shows that the tunneling current I_{tunnel}

between the two layers is negligible and cannot compromise the drag measurements (45). This contrasts with the nonequilibrium exciton fluid reported by Wang *et al.* (24), in which the observed I_{tunnel} was orders of magnitude higher.

The bottom panel of Fig. 3A shows the drag current ratio, $I_{\text{drag}}/I_{\text{drive}}$, at 1.5 K. It displays perfect Coulomb drag in the EI region and negligible Coulomb drag ($I_{\text{drag}}/I_{\text{drive}} < 0.001$) for pair density above n_M . The temperature and pair density dependences of the drag current ratio are summarized in Fig. 3B, and representative density line cuts are illustrated in Fig. 3C. In general, Coulomb drag decreases with increasing temperature and pair density except for the region near n_M at low temperatures, where the temperature dependence is nonmonotonic. A large drag current ratio remains above 0.9 up to about 20 K at low pair densities.

When exciton transport dominates over free carrier transport in the channel, perfect Coulomb

drag is expected because a steady current of electrons driven through one layer must be accompanied by an equal current of holes in the other layer (3). By contrast, when the electrons and holes are unbound, only small frictional drag is expected (42). In the case of Fermi liquids, the phase space of electrons and holes available for Coulomb drag increases with temperature, and the drag current ratio scales quadratically with temperature at low temperatures (42). The observed perfect Coulomb drag in our experiment therefore demonstrates the dominance of exciton transport in the EI region at low temperatures. Its temperature dependence can be largely captured by a simple model (Fig. 3C, solid lines) of exciton thermal dissociation (48), in which the frictional drag and the contact resistance of the drag layer are ignored and the exciton-to-charge carrier mobility ratio is the only fitting parameter and is assumed to be temperature independent (45). (These simple assumptions likely cause the observed discrepancy between experiment and theory at low temperatures.) The excitons can also be ionized into an electron-hole plasma at low temperatures by the state filling effect when the pair density exceeds the Mott density (2, 48). The latter corresponds to the abrupt vanishing of the drag current near n_M at low temperatures, where n_M is the Mott density (we estimate $n_M a_B^2 \approx 0.4$, with a_B denoting the exciton Bohr radius). Above the Mott density, the negligible Coulomb drag at 1.6 K implies near-complete exciton ionization; $I_{\text{drag}}/I_{\text{drive}}$ increases quadratically with temperature at low temperatures by the phase space argument ($n_p = 6 \times 10^{11}$; Fig. 3C).

EI-to-metal transition

We measure the drag resistance of our devices to directly probe the transition from an EI to an electron-hole plasma using the open-circuit geometry shown in Fig. 1D. We bias I_{drive} in the Mo layer and measure the drag voltage drop in the W layer, V_{drag} , using a voltmeter with 100-megohm input impedance. The drag resistance, $R_{\text{drag}} = V_{\text{drag}}/I_{\text{drive}}$, reflects the charge resistance of the double layer (see the circuit model in fig. S1D) (45). It is closely connected to the drag current described above. In the EI region at low temperatures (where the exciton conductivity is expected to far exceed the charge conductivity and the frictional drag conductivity), the two quantities are related, $\frac{I_{\text{drag}}}{I_{\text{drive}}} = \frac{1}{1+R_{\text{WC}}/R_{\text{drag}}}$, by the contact resistance (R_{WC}) in the drag layer (fig. S1F). The good agreement between the measured drag current ratio and the inferred one from R_{drag} using $R_{\text{WC}} \approx 7 \text{ kilohm}$ (fig. S7) supports the validity of this simple relation for a wide range of temperatures and pair densities. The contact resistance is also independently verified by the two-terminal resistance measurement in the W layer (fig. S5).

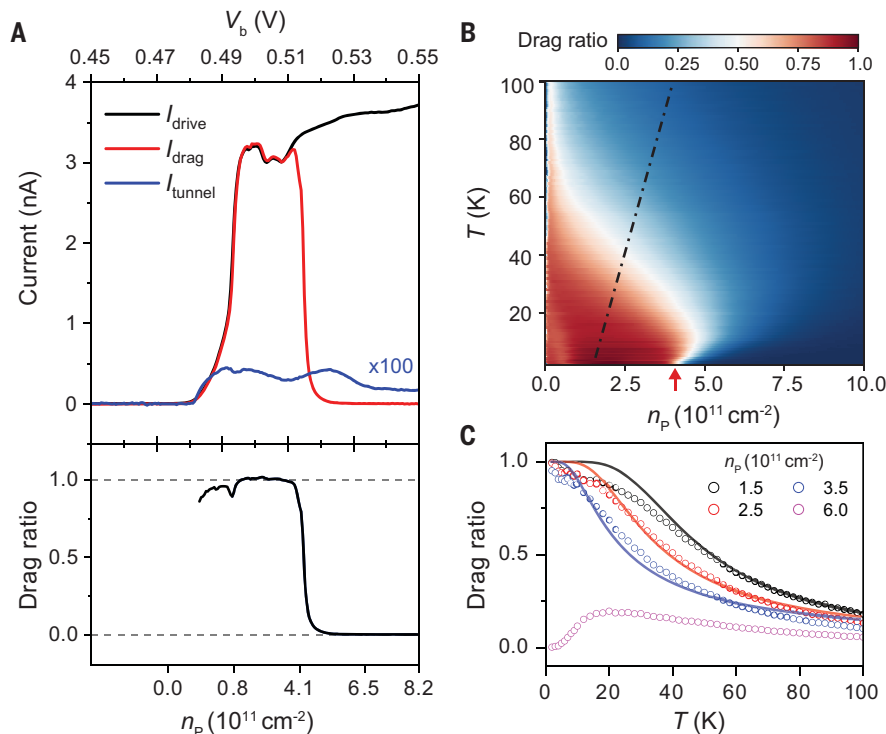


Fig. 3. Perfect Coulomb drag. (A) (Top) Drive current, drag current, and tunneling current (multiplied by 100) as a function of V_b (upper axis) and pair density n_p (lower axis) at 1.5 K. (Bottom) The corresponding drag current ratio. Pair density is calibrated from the interlayer capacitance with a systematic uncertainty of $\sim 0.5 \times 10^{11} \text{ cm}^{-2}$. Perfect drag is observed in the EI region, where the tunneling current is negligible. The drag current ratio quickly drops to zero outside the EI region. (B) Drag current ratio as a function of pair density n_p and temperature T . The dotted-dashed line marks the degeneracy temperature T_d , evaluated from the exciton compressibility peak. The red arrow denotes the Mott density, $n_M \approx 4.0 \times 10^{11} \text{ cm}^{-2}$. (C) Temperature dependence of the drag current ratio at selected pair densities. Empty symbols and solid lines are the experimental data and the theoretical fits described in the main text and the supplementary materials (45), respectively. The drag current ratio remains above 0.9 at low pair densities up to about 20 K. All data were acquired along the white dashed line in Fig. 2A.

Figure 4A shows the temperature dependence of R_{drag} at varying pair densities. As temperature decreases, R_{drag} increases for small densities (an insulating behavior) and decreases for large densities (a metallic behavior). A variation in R_{drag} by nearly six orders of magnitude is observed at 1.5 K. On the metallic side, a Fermi liquid frictional drag, $R_{\text{drag}} \approx AT^2$, is observed in the low-temperature limit (42, 49) (fig. S6); a nonmonotonic temperature dependence is also visible near the Mott density. The nonmonotonic dependence demonstrates a crossover from a low-temperature coherent transport regime to a high-temperature incoherent (or classical) regime that occurs near the Fermi temperature of the TMD monolayers (50). The Fermi temperature (near the R_{drag} maximum) vanishes continuously as pair density approaches n_M from the metallic side. Notably, such a nonmonotonic dependence has been qualitatively captured in earlier theoretical studies (51–53), which take into account density- and temperature-dependent screening of electron-hole binding near the exciton Mott transition.

We further analyzed the observed insulator-to-metal transition following the procedures outlined by Dobrosavljevic *et al.* (54). We first identified the resistance curve at the critical density, R_c , as the one that displays a power-law temperature dependence (Fig. 4A, dashed line); the corresponding density agrees well with the Mott density. We then normalized the temperature-dependent R_{drag} at other densities by R_c . We can collapse all the normalized resistances into two groups with insulating and metallic behavior, respectively, by normalizing T using a density-dependent temperature T_0 (Fig. 4A, inset). The parameter T_0 vanishes continuously toward n_M from both sides (fig. S9). It is well correlated with the EI charge gap $[\approx (C_P/C_{\text{gg}})dV_g]$ obtained from the penetration capacitance measurement on the insulating side (Fig. 4B). In Fig. 4B, we summarize the coefficient A from fitting the temperature-dependent R_{drag} to AT^2 at low temperatures on the metallic side. The coefficient increases by three orders of magnitude as pair density approaches n_M . Together, the continuously vanishing charge gap (and T_0) and the diverging A coefficient with pair density approaching the Mott density from two sides suggest a possible continuous EI-to-metal transition (55).

We also observed that the coefficient A scales with pair density as $A \propto (n_p - n_M)^{-3}$ (Fig. 4B, solid line). This resembles, but at the same time differs from, the theoretical prediction of $A \propto (n_p)^{-3}$ for frictional drag from the interlayer Coulomb scattering (42, 56). The reset of the pair density by the Mott density suggests a diverging electron/hole effective mass at n_M (42, 56), consistent with the vanishing electron/hole Fermi temperature at n_M discussed above.

The reset is beyond the current understanding. Future theoretical studies taking into account the BEC-BCS crossover (57) and the possible Mott transition at n_M are needed to understand the density dependence of A (BEC and BCS stand for Bose-Einstein condensation and Bardeen-Cooper-Schrieffer, respectively).

Discussion and outlook

We illustrate the experimental phase diagram for the exciton fluid in Fig. 3B. The degeneracy temperature T_d (Fig. 3B, dashed line) is obtained from the exciton compressibility peak in the temperature-dependent interlayer capacitance measurement (15, 58–60). The exciton fluid is in the degenerate quantum limit below T_d . The degeneracy temperature (21) is substantially enhanced by the strong exciton-exciton interactions (15, 60). The exciton fluid is also expected to transition to a superfluid at the Berezinskii-Kosterlitz-Thouless transition temperature lower than T_d (21, 60). However, the Coulomb drag measurements are insensitive to spontaneous phase coherence and superfluid phase transition. The seemingly continuous exciton Mott transition near n_M observed in our experiment is inconsistent with mean-field theories (21, 22, 67), which have predicted an abrupt transition. On the other hand, density matrix renormalization group (DMRG) and random phase approximation (RPA) with dynamical screening methods have suggested a smooth crossover with exponentially suppressed exciton binding near n_M (57, 62), which

would explain an insulator-to-metal transition at finite temperatures but cannot explain the $A \propto (n_p - n_M)^{-3}$ divergence near n_M . The nature of the exciton Mott transition remains to be settled by further theoretical and experimental studies.

Finally, we comment on the effect of disorders. The disorder density in monolayer TMDs is estimated to be $n_d \approx 10^{11} \text{ cm}^{-2}$ (fig. S13). (It is expected to be lower in the double layers because of extra screening of the disorder potentials by the other TMD layer.) The excitons are expected to be localized for $n_p < n_d$; they become delocalized (and possibly a superfluid) for $n_d < n_p < n_M$. This density window for interesting bosonic phases of matter can be further enlarged by a perpendicular magnetic field that strengthens the exciton binding (fig. S16).

We have demonstrated perfect Coulomb drag at low temperatures, with the drag current ratio remaining above 0.9 up to about 20 K, in a gate-tunable EI realized in TMD atomic double layers separated by a thin hBN barrier. The drag resistance measurement has further revealed an EI-to-metal transition at the Mott density. These studies are enabled by successfully establishing separate electrical contacts to the electron and hole components of the EI. The perfect Coulomb drag demonstrates pure exciton transport across the EI. However, the relatively large contact resistance in the Mo layer of the current devices hinders settling whether the exciton transport is dissipationless

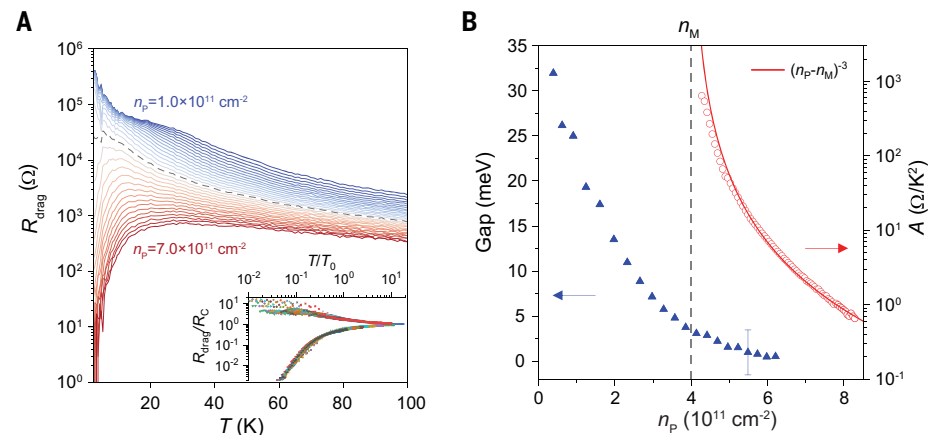


Fig. 4. EI-to-metal transition. (A) Temperature dependence of the drag resistance at varying pair densities n_p from 1 to $7 \times 10^{11} \text{ cm}^{-2}$ with a step size of $0.2 \times 10^{11} \text{ cm}^{-2}$. The critical resistance curve R_c (dashed line) at the Mott density $n_M \approx 4.0 \times 10^{11} \text{ cm}^{-2}$ separates the insulating behavior at low pair densities and the metallic behavior at high pair densities. (Inset) Critical scaling of resistance around n_M . The temperature-dependent resistances normalized by R_c collapse into two groups (with insulating and metallic behavior) when the temperature is scaled by a density-dependent temperature T_0 . (B) EI charge gap (filled triangles) and coefficient A (empty circles) as a function of pair density n_p . The charge gap is obtained from the penetration capacitance measurement (45); the error bar represents the systematic uncertainty induced by the finite ac bias voltage in the measurement. The coefficient A is obtained by fitting the temperature-dependent frictional drag ($R_{\text{drag}} = AT^2$) for $n_p > n_M$ (fig. S6). The solid red line plots the scaling $A \propto (n_p - n_M)^{-3}$. The vertical dashed line marks the Mott density n_M .

—that is, whether there is exciton superfluidity. Future four-exciton terminal measurements that can drive an exciton current and simultaneously measure the exciton chemical potential drop along the channel should be able to set a limit on dissipation occurring in the exciton channel.

REFERENCES AND NOTES

1. D. Jérôme, T. M. Rice, W. Kohn, *Phys. Rev.* **158**, 462–475 (1967).
2. N. F. Mott, *Philos. Mag.* **6**, 287–309 (1961).
3. D. Nandi, A. D. K. Finck, J. P. Eisenstein, L. N. Pfeiffer, K. W. West, *Nature* **488**, 481–484 (2012).
4. L. Tiemann *et al.*, *Phys. Rev. B* **77**, 033306 (2008).
5. J. P. Eisenstein, A. H. MacDonald, *Nature* **432**, 691–694 (2004).
6. X. Liu, K. Watanabe, T. Taniguchi, B. I. Halperin, P. Kim, *Nat. Phys.* **13**, 746–750 (2017).
7. Y. Zeng *et al.*, Evidence for a Superfluid-to-solid Transition of Bilayer Excitons. arXiv:2306.16995 [cond-mat.mes-hall] (2023).
8. J. I. A. Li, T. Taniguchi, K. Watanabe, J. Hone, C. R. Dean, *Nat. Phys.* **13**, 751–755 (2017).
9. X. Liu *et al.*, *Science* **375**, 205–209 (2022).
10. J. A. Seamons, C. P. Morath, J. L. Reno, M. P. Lilly, *Phys. Rev. Lett.* **102**, 026804 (2009).
11. A. Gamucci *et al.*, *Nat. Commun.* **5**, 5824 (2014).
12. A. F. Croxall *et al.*, *Phys. Rev. Lett.* **101**, 246801 (2008).
13. J. I. A. Li *et al.*, *Phys. Rev. Lett.* **117**, 046802 (2016).
14. K. Lee *et al.*, *Phys. Rev. Lett.* **117**, 046803 (2016).
15. L. Ma *et al.*, *Nature* **598**, 585–589 (2021).
16. R. Qi *et al.*, *Nat. Commun.* **14**, 8264 (2023).
17. Z. Sun, T. Kaneko, D. Golež, A. J. Millis, *Phys. Rev. Lett.* **127**, 127702 (2021).
18. A. V. Balatsky, Y. N. Joglekar, P. B. Littlewood, *Phys. Rev. Lett.* **93**, 266801 (2004).
19. J. Hu, A. F. Rigosi, D. B. Newell, Y. P. Chen, *Phys. Rev. B* **102**, 235304 (2020).
20. S. K. Banerjee, L. F. Register, E. Tutuc, D. Reddy, A. H. MacDonald, *IEEE Electron Device Lett.* **30**, 158–160 (2009).
21. M. M. Fogler, L. V. Butov, K. S. Novoselov, *Nat. Commun.* **5**, 4555 (2014).
22. F.-C. Wu, F. Xue, A. H. MacDonald, *Phys. Rev. B* **92**, 165121 (2015).
23. M. Xie, A. H. MacDonald, *Phys. Rev. Lett.* **121**, 067702 (2018).
24. Z. Wang *et al.*, *Nature* **574**, 76–80 (2019).

25. G. W. Burg *et al.*, *Phys. Rev. Lett.* **120**, 177702 (2018).
26. B. I. Halperin, T. M. Rice, *Rev. Mod. Phys.* **40**, 755–766 (1968).
27. L. V. Keldysh, Y. V. Kopaev, *Fiz. Tverd. Tela* **6**, 2791–2798 (1964).
28. J.-J. Su, A. H. MacDonald, *Nat. Phys.* **4**, 799–802 (2008).
29. Y. E. Lozovik, V. I. Yudson, *Sov. Phys. JETP* **44**, 389–397 (1976).
30. X. Zhu, P. B. Littlewood, M. S. Hybertsen, T. M. Rice, *Phys. Rev. Lett.* **74**, 1633–1636 (1995).
31. L. V. Butov, *J. Phys. Condens. Matter* **16**, R1577–R1613 (2004).
32. P. López Ríos, A. Perali, R. J. Needs, D. Neilson, *Phys. Rev. Lett.* **120**, 177701 (2018).
33. S. Conti *et al.*, *Phys. Rev. Lett.* **130**, 057001 (2023).
34. Y. N. Joglekar, A. V. Balatsky, S. Das Sarma, *Phys. Rev. B* **74**, 233302 (2006).
35. M. A. Baranov, M. Dalmonte, G. Pupillo, P. Zoller, *Chem. Rev.* **112**, 5012–5061 (2012).
36. H. Cercellier *et al.*, *Phys. Rev. Lett.* **99**, 146403 (2007).
37. A. Kogar *et al.*, *Science* **358**, 1314–1317 (2017).
38. Y. Wakasaka *et al.*, *Phys. Rev. Lett.* **103**, 026402 (2009).
39. L. Du *et al.*, *Nat. Commun.* **8**, 1971 (2017).
40. B. Sun *et al.*, *Nat. Phys.* **18**, 94–99 (2022).
41. Y. Jia *et al.*, *Nat. Phys.* **18**, 87–93 (2022).
42. B. N. Narozhny, A. Levchenko, *Rev. Mod. Phys.* **88**, 025003 (2016).
43. J. Wang *et al.*, *Phys. Rev. Lett.* **126**, 106804 (2021).
44. J. Wang *et al.*, *Sci. Adv.* **5**, eaax0145 (2019).
45. See the supplementary materials for details.
46. D. D. Dai, L. Fu, *Phys. Rev. Lett.* **132**, 196202 (2024).
47. I. Amelio, N. D. Drummond, E. Demler, R. Schmidt, A. Imamoglu, *Phys. Rev. B* **107**, 155303 (2023).
48. G. Mancke, D. Semkat, H. Stolz, *New J. Phys.* **14**, 095002 (2012).
49. R. V. Gorbachev *et al.*, *Nat. Phys.* **8**, 896–901 (2012).
50. S. Das Sarma, E. H. Hwang, *Phys. Rev. B* **68**, 195315 (2003).
51. D. Semkat *et al.*, *Phys. Rev. B* **80**, 155201 (2009).
52. D. Snoke, *Solid State Commun.* **146**, 73–77 (2008).
53. K. Asano, T. Yoshioka, *J. Phys. Soc. Jpn.* **83**, 084702 (2014).
54. V. Dobrosavljevic, N. Trivedi, J. M. Valles, Eds., *Conductor-Insulator Quantum Phase Transitions* (Oxford Univ. Press, 2012).
55. T. Li *et al.*, *Nature* **597**, 350–354 (2021).
56. E. H. Hwang, R. Sensarma, S. Das Sarma, *Phys. Rev. B* **84**, 245441 (2011).
57. D. Vu, S. Das Sarma, *Phys. Rev. B* **108**, 235158 (2023).
58. Yu. Kagan, V. A. Kashurnikov, A. V. Krasavin, N. V. Prokof'ev, B. V. Svistunov, *Phys. Rev. A* **61**, 043608 (2000).

59. Y. E. Lozovik, I. L. Kurbakov, G. E. Astrakharchik, J. Boronat, M. Willander, *Solid State Commun.* **144**, 399–404 (2007).
60. Z. Hadzibabic, J. Dalibard, *Riv. Nuovo Cim.* **34**, 389–434 (2011).
61. V. V. Nikolaev, M. E. Portnoi, *Superlattices Microstruct.* **43**, 460–464 (2008).
62. G. J. Sreejith, J. D. Sau, S. Das Sarma, *Phys. Rev. Lett.* **133**, 056501 (2024).
63. P. X. Nguyen *et al.*, Perfect Coulomb drag in a dipolar excitonic insulator, dataset, Zenodo (2025).

ACKNOWLEDGMENTS

We thank A. MacDonald, L. Fu, S. Das Sarma, P. Littlewood, and E. Mueller for fruitful discussions. **Funding:** This work was supported by the US National Science Foundation (NSF) under DMR-2004451 (capacitance measurement) and the Department of Energy (DOE), Office of Science, Basic Energy Sciences (BES), under award no. DE-SC0022058 (transport measurement). It was also funded in part by the Gordon and Betty Moore Foundation (grant no. GBMF1563). Growth of the hBN crystals was supported by the Elemental Strategy Initiative of MEXT, Japan and CREST (JPMJCR15F3), JST. This work was performed in part at the Cornell NanoScale Science and Technology Facility, a National Nanotechnology Coordinated Infrastructure (NNCI) member supported by NSF grant NNCI-2025233. We also acknowledge support from the David and Lucille Packard Fellowship (K.F.M.) and the Kavli Institute at Cornell (KIC) Engineering Graduate Fellowship (P.X.N.). **Author contributions:** P.X.N., L.M., and R.C. fabricated the devices, performed the measurements, and analyzed the data. K.W. and T.T. grew the bulk hBN crystals. K.F.M. and J.S. designed the scientific objectives and oversaw the project. All authors discussed the results and commented on the paper. **Competing interests:** The authors declare no competing interests. **Data and materials availability:** All data shown in the main text and supplementary materials are available in the Zenodo data repository (63). **License information:** Copyright © 2025 the authors, some rights reserved; exclusive licensee American Association for the Advancement of Science. No claim to original US government works. <https://www.science.org/about/science-licenses-journal-article-reuse>

SUPPLEMENTARY MATERIALS

science.org/doi/10.1126/science.adl1829
Materials and Methods
Supplementary Text
Figs. S1 to S19
References (64–68)

Submitted 3 October 2023; accepted 25 February 2025
10.1126/science.adl1829